da Silva *et al. Energy Mater* 2024;4:400058
DOI: 10.20517/energymater.2023.114

Energy Materials

Article

Open Access

Check for updates

X-ray dose effects and strategies to mitigate beam damage in metal halide perovskites under high brilliance X-ray photon sources

Francisco M. C. da Silva[1,2], Rodrigo Szostak[1,*], Maria G. D. Guaita[1,3], Verônica C. Teixeira[1], Ana F. Nogueira[3], Hélio C. N. Tolentino[1,*]

[1]Brazilian Synchrotron Light Laboratory (LNLS), Brazilian Center for Research in Energy and Materials (CNPEM), Campinas, SP 13083-970, Brazil.
[2]Physics Institute (IFGW), University of Campinas (UNICAMP), Campinas, SP 13083-970, Brazil.
[3]Laboratório de Nanotecnologia e Energia Solar (LNES), Chemistry Institute (IQ), University of Campinas (UNICAMP), Campinas, SP 13083-970, Brazil.

***Correspondence to:** Dr. Rodrigo Szostak, Brazilian Synchrotron Light Laboratory (LNLS), Brazilian Center for Research in Energy and Materials (CNPEM), Rua Giuseppe Máximo Solfaro, 10000, Campinas, SP 13083-100, Brazil. E-mail: rodrigo.szostak@lnls.br; Dr. Hélio C. N. Tolentino, Brazilian Synchrotron Light Laboratory (LNLS), Brazilian Center for Research in Energy and Materials (CNPEM), Rua Giuseppe Máximo Solfaro, 10000, Campinas, SP 13083-100, Brazil. E-mail: helio.tolentino@lnls.br

How to cite this article: da Silva FMC, Szostak R, Guaita MGD, Teixeira VC, Nogueira AF, Tolentino HCN. X-ray dose effects and strategies to mitigate beam damage in metal halide perovskites under high brilliance X-ray photon sources. *Energy Mater* 2024;4:400058. https://dx.doi.org/10.20517/energymater.2023.114

Received: 23 Dec 2023 **First Decision:** 10 Apr 2024 **Revised:** 8 May 2024 **Accepted:** 22 May 2024 **Published:** 6 Jun 2024

Academic Editors: Meicheng Li, Weihua Tang **Copy Editor:** Fangyuan Liu **Production Editor:** Fangyuan Liu

Abstract

Metal halide perovskites (MHP) suffer from photo-structural-chemical instabilities whose intricacy requires state-of-the-art tools to investigate their properties under various conditions. This study addresses the damage caused by focused X-ray beams on MHP through a correlative multi-technique approach. The damage after high-dose irradiation is noticeable in many ways: the loss of iodine and organic components, whose relative amount is reduced; the formation of an excavated area modifying the sample morphology; and an altered optical reflectivity indicating an optically inactive layer. The damage mechanism combines radiolysis and sputtering processes. Interestingly, the bulk underneath the excavated area maintains the initial halide proportion demonstrated by a stable photoluminescence emission energy. We also show that controlling the beam dose and environment is an excellent strategy to mitigate the dose harm. Hence, we combined a controlled X-ray dose with an inert N_2 atmosphere to certify the conditions to probe MHP properties while mitigating damage efficiently. Finally, we

applied optimized conditions in an X-ray ptychography experiment, reaching a 15-nm spatial resolution, an outcome that has never been attained in this class of materials.

Keywords: Metal halide perovskites, X-ray beam damage, perovskite solar cells, synchrotron radiation, X-ray nanoprobe

INTRODUCTION

Metal halide perovskite (MHP) materials have received enormous attention due to their photovoltaic and optoelectronic properties suitable for solar cells[1,2], photonic devices[3,4], and X-ray detectors[5]. However, many aspects of their properties must be uncovered to move their technologies from lab to market[6]. The MHP instabilities under operation and the correlated photo-structural-chemical transformations require advanced characterization tools coupled with *in situ* and *operando* experiments for a comprehensive nanoscale view[7]. X-ray fluorescence (XRF)[8], X-ray diffraction (XRD)[9,10], X-ray beam-induced current (XBIC)[11], X-ray excited optical luminescence (XEOL)[12] and coherent diffraction imaging (CDI)[13] with focused beams are increasingly sophisticated and accessible at fourth-generation synchrotron sources, becoming powerful tools to investigate MHPs, or even complete perovskite solar cells (PSCs). Nevertheless, in most cases, those tools strongly interact with the materials, leading to undesirable transformations. Although promising, focused X-ray-based techniques face high radiation doses deposited on the samples, which may cause damage to the materials and devices, altering their properties. Stuckelberger *et al.* showed that the electronic properties of the perovskite are the most sensitive, leading to a drastic reduction of the XBIC signal under X-ray irradiation but with no evidence of the element's composition changes[14]. X-ray photoemission (XPS) experiments also demonstrated the sensibility of the electronic properties, suggesting that the organic part of the perovskite [formamidinium (FA) and methylammonium (MA)] suffer radiolysis, producing volatile species[15,16]. Ferrer Orri *et al.* revealed that the degradation mechanism for electrons and X-rays is similar and is probably caused by the interaction of electrons, also generated by the X-rays, with the organic part of the MHP. In defective grain boundaries, even low doses of electrons change grain orientations[17]. Also, the degradation seems to be facet-dependent, indicating that the sample crystalline quality is crucial to the resilience to X-ray damage[18]. Interestingly, the cryogenic conditions do not avoid degradation but favor sample amorphization[19,20]. Conversely, temperatures around 90 °C do not induce additional severe perovskite degradation[19]. Besides the critical insights already uncovered, a comprehensive investigation of several X-ray dose aspects on the morphological, structural, and chemical properties of the MHP films extensively applied in PSC devices remains missing.

This work uses a correlative multi-technique approach to investigate the effect of the focused X-ray beam on the element's distribution, morphology, structure, and optoelectronic properties of the $[(FAPbI_3)_{0.87}(MAPbBr_3)_{0.13}]_{0.92}(CsPbI_3)_{0.08}$ ($CsFAMAPb(Br,I)_3$) compound. Such composition is relevant because it is widely used in fundamental studies and devices and presents a mixture of the main elements/molecules used in MHP. We irradiated the samples with controlled X-ray doses under different atmospheres and temperatures and evaluated the damage using correlative multiple micro and nanoscale techniques. The correlative data showed that the X-ray dose caused damage on the exposed surface, mainly affecting the iodine and organic elemental components, leading to topographical changes by ejecting material and forming an excavated area. The local optical reflectivity within this area indicates the formation of a metallic layer coating the surface. Surprisingly, the bulk compound underneath the excavated area preserved its optoelectronic properties. As expected, decreasing the X-ray dose and using an inert atmosphere reduced the damage. However, selective ejection seems to be independent of the temperature conditions. We demonstrate that combining an inert atmosphere with a controlled dose reduction at room temperature is the way to investigate hybrid organic-inorganic MPHs with state-of-the-art X-ray nanoprobes. Finally, we applied the optimized conditions below the critical dose to demonstrate the

feasibility of studying MHPs with the X-ray ptychography (CDI) technique to highlight the grain morphology and sample details with a 15-nm spatial resolution. Such a technique had never been reported before in this class of compounds.

EXPERIMENTAL

Sample preparation

The CsFAMAPb(I,Br)$_3$ perovskite with composition $[(FAPbI_3)_{0.87}(MAPbBr_3)_{0.13}]_{0.92}(CsPbI_3)_{0.08}$ was deposited using the antisolvent method on polished Si substrates covered with 100 nm of Au. The substrates were cleaned with isopropanol and ultraviolet-ozone (UVO) treated for 30 min before the deposition. The perovskite solution was prepared using FAI (GreatCell Solar Materials), MABr (GreatCell Solar Materials), PbI_2 (TCI America), $PbBr_2$ (TCI America), and CsI (TCI America) with a concentration of 0.7 M regarding Pb component. The powders were dissolved in a mixture of anhydrous N, N-dimethylformamide (DMF, Sigma-Aldrich) and dimethyl sulfoxide (DMSO, Sigma-Aldrich) with a volume ratio of DMF:DMSO = 4:1 at room temperature. The solution was spin-coated at 2,000 rpm for 12 s followed by 5,000 rpm for 30 s. Additionally, 15 s before the end of the spin-coating, 150 µL of chlorobenzene was dropped on the film. After deposition, the substrates were thermal annealed for 60 min at 100 °C. The $Cs_{0.05}FA_{0.95}PbI_3$ was deposited by the gas quenching method on the Mylar substrate[21]. The substrates were cleaned with UVO treated for 30 min before deposition. The perovskite precursor solution was prepared by solubilizing CsI (TCI America), FAI (GreatCell Solar Materials), PbI_2 (TCI America), and 40 mol% of MACl, with an excess of 5% of the lead source in the mixture of solvents DMF (Sigma-Aldrich) and methylpyrrolidone (NMP, Sigma-Aldrich) (v:v = 4:1) with a concentration of 1.3 M. The solution was spin-coated at 4,000 rpm for 60 s. A jet of N_2 was automatically blown during the final 50 s of the rotation to force the solvent's exit and the perovskite's subsequent crystallization. The film was then heated in the air at 100 °C for 90 min.

Synchrotron experiments

The sample CsFAMAPb(I, Br)$_3$ was used for all the experiments except for the ptychography measurements performed on the $Cs_{0.05}FA_{0.95}PbI_3$ sample. For the same environment condition [room temperature and air atmosphere (RT-Air), RT and nitrogen flow (RT-N_2), or cryogenic temperature (152 K) and N_2 flow (Cryo-N_2)], all X-ray measurements were performed in the same compound deposited on an Au-coated Si substrate, with a total size of ≈ 10 × 10 mm, which was cut into small pieces. Three pieces were selected, each used for a different environmental condition. Various areas spaced by 50 µm were measured, forming an array with distinct doses. The samples were exposed to the 500 × 200 nm^2 X-ray beam and raster-scanned in a fly scan mode at the Tarumã station of the Carnaúba beamline[22]. In the fly scan mode, the beam is continuously scanned on the sample while the signal is recorded. For instance, when the beam scans a distance of 10 µm and 100 points are recorded, each point corresponds to a step of 100 nm. For easier reporting, we refer to it as steps of the fly scan. An XRF spectrum is collected for each (x, y) coordinate. The X-ray beam irradiated the samples at 10 and 14 keV to collect the XRF data. The nano-XRF maps were obtained using custom-made Python scripts that integrated the selected XRF peak emissions. The maps were obtained in the emissions I-Lα1 (3,938 eV), Pb-Lα1(10,551 eV) and Br-Kα1(11,924 eV). Supplementary Figure 1 shows XRF spectra for the 10 and 14 keV and corresponding peaks used to obtain the maps. The 10-keV irradiation induced beam damage and obtained the I maps. The 14-keV irradiation was used to attain the Pb and Br maps. For the RT-N_2 and Cryo-N_2 experiments, the cryogenic sample environment was used with a constant flow of N_2 at room temperature and a cold N_2, respectively[23]. After the synchrotron experiments, the samples were stored in a dry box with a drying agent until further studies. The X-ray doses were controlled using three different X-ray fly scan settings, covering an area of 5 µm × 5 µm. For 2.9 GGy, the step size was 200 nm, and the exposure time was 750 ms by point. For 1.9 GGy, the step size was 60 nm with an exposure time of 58 ms. For 0.7 GGy, the step size was 50 nm, and the exposure time of 8 ms. Then, the irradiated areas were inspected with a 10 µm × 10 µm scan, step size of 100

nm, and exposure time of 7.5 ms. More details about the scans can be found in Supplementary Table 1. The ratio of the iodine reduction was calculated by the average intensity of a 2 × 2 μm^2 area at the center of the irradiated area, compared to a similar area outside the irradiated region. The ratio presents an error of ±15%, estimated from several images due to statistical fluctuation.

Ptychography measurements and analysis

An X-ray ptychography experiment involves illuminating a sample with a coherent beam, systematically scanning it with overlap between the probed regions, and recording continuous diffraction patterns associated with each position. The collected diffraction patterns are then computationally processed to reconstruct high-resolution images (not limited by the probe size but by the numerical aperture collected in the detector) of both the amplitude and phase of the sample. The non-destructive nature and enhanced contrast of ptychography have enabled breakthroughs in materials science, biology, and nanotechnology, mainly due to its suitability for challenging low-absorption contrast materials[24-26]. Typical experimental constraints include beam coherence, sample stability, sample preparation, and the detector specifications.

In our experiments, 10100 positions were recorded in an area of 10 × 10 μm^2 (step of 100 nm; probe size of (200 × 500) H × V nm^2, overlap > 50%, including random variations in the probe positions to a perfect square grid)[27]. The scan was performed at the energy of 10 keV in fly-scan mode with a constant velocity of 10 μm/s, giving a total acquisition time of 172 s. The total dose of the scan was estimated to be 0.0015 GGy. For the reconstruction, 180 × 180 pixels (55 × 55 μm^2) of the data PiMega area detector at the distance of 1.1 m from the sample were used, resulting in a pixel size of reconstruction of 13.7 nm. The object was initialized with random amplitude and phase maps. The probe was initialized with the inverse Fourier transform of the average of the diffraction patterns in the first mode. Six more modes were added as random fluctuations of the first mode, and their maximum intensities were normalized to 15% of the first mode. The reconstruction was performed by combining 100 iterations of the Alternating projections (AP)[28] algorithm, followed by 5,000 iterations of the Relaxed averaged alternating reflections (RAAR)[29] method, and finally, 1,000 iterations of AP. The final R factor of the reconstruction reached the value of 5.30%[30,31].

μ-FTIR

The X-ray irradiated areas were identified by optical microscopy coupled with the Fourier-transform infrared micro-spectroscopy (μ-FTIR) equipment and then measured. The experiments were performed at the Infrared Micro and Nanospectroscopy (IMBUIA) beamline of the Brazilian Synchrotron Light Laboratory (LNLS) at the IMBUIA-Micro station. A blackbody infrared (IR) source in a commercial IR spectral microscope was used. The images were obtained using a focal plane array (FPA) IR detector with 256 scans and a spectral resolution of 8 cm^{-1}. The μ-FTIR maps were obtained by custom-made Python scripts integrating the selected IR peak signals.

AFM

The atomic force microscopy (AFM) data were acquired at the In situ Growth Laboratory (LCIS) of the LNLS, which is part of the Brazilian Center for Research in Energy and Materials (CNPEM). The images were obtained using a Nanosurf Flex AFM. Scans covered an area of 10 × 10 μm^2 with a step size of 20 nm at dynamic force contact mode with the cantilever type Tap 300-AI-G with 1.5 s per line. The data were analyzed with the Gwyddion software. The images here correspond to the morphology acquired in the Z-axis forward direction. The Z-axis backward direction images were checked to exclude possible artifacts.

μ-PL

The micro-photoluminescence (μ-PL) data were acquired at the Brazilian Nanotechnology National Laboratory (LNNano), part of the CNPEM. The PL was obtained using a confocal Raman spectrometer

Horiba XploRA plus. The damaged X-ray areas were found using optical microscopy coupled to the equipment, and then PL measurements were obtained in different regions with a beam size of around 1 μm. The excitation source was a 638 nm laser with a minimum power of 0.1% and a minimum integration time of 10 ms. The microscope optical system eliminates the laser scattering at a wavelength < 640 nm.

Optical microscopy

The optical microscopy images were acquired at the Laboratory of Microscopic Samples (LAM) of the LNLS, part of the CNPEM. The images were obtained using a Nikon Eclipse LV100-UDM-POL microscope with a magnification of 100×. The colors in the image represent the real colors of the surface.

Methodology

We deposited the perovskite CsFAMAPb(Br, I)$_3$ using the traditional antisolvent method onto Si/Au substrates (see details in the experimental section). This substrate is well-suited for this study because it allows X-ray and other correlative characterization techniques, such as μ-FTIR, AFM, and μ-PL. The X-ray beam damage was investigated at the CARNAÚBA X-ray Nanoprobe beamline of the LNLS/CNPEM[22]. The Sirius storage ring was running at 3 GeV and 100 mA[32], with the beamline delivering a nanobeam of 200 nm(V) × 500 nm(H) and a photon flux of 5 × 109 ph/s at 10 keV. The methodology to collect information on damage consisted of irradiating a small portion of the sample (5 × 5 μm^2) with controlled X-ray doses and environmental conditions, then mapping the previously irradiated area employing reduced X-ray doses over a larger area (10 × 10 μm^2). Fiducial marks on the samples allowed them to transfer to other instruments to perform correlative measurements.

RESULTS AND DISCUSSION

Figure 1A shows the nano-XRF map of the iodine emission of a 5 × 5 μm^2 irradiated area acquired at the RT-Air condition. To irradiate and map the sample, we used the fly-scan snake mode with the scan starting on the left-bottom corner of the image and the beam spot going up and down while sliding to the right related to the sample. The X-ray dose after irradiation corresponds to 2.9 GGy deposited in the scanned region, where 1 Gy = 1 J/kg is a measure of the total energy deposited per quantity of material irradiated[33,34]. The estimated dose considers the total absorption of the compound at the irradiation energy so that doses deposited using distinct X-ray energies can be appropriately compared. The total amount of absorbed 10-keV photons by the 330-nm-thick perovskite film corresponds to 2.53 × 10^{21} ph/m^2. We present the dose calculation and its Python code in the Supplementary Information (SI).

The decreasing iodine XRF emission in the irradiated region is observed in Figure 1B. To inspect this irradiated region, we performed a larger scan of 10 × 10 μm^2 centered at the same point as the previous 5 × 5 μm^2 scan but with a much lower dose. The dose for the measurement corresponds to about 0.2 GGy in the scanned region, representing about 7% of the dose used for the irradiation. The iodine map reveals a reduction of the number of iodine atoms in a square with the exact dimension of the previously irradiated region. The average fluorescence counts correspond to about a 28% decrease. Interestingly, the Pb and Br maps do not show any evidence of composition changes [Figure 1C and D]. A noticeable additional effect [Figure 1A] is the decreasing iodine XRF emission from left to right in the scan direction. This gradient is not fortuitous but is systematically observed in various samples under high doses [Supplementary Figure 2]. As the horizontal nanoprobe size (500 nm) is larger than the fly scan step (200 nm), the initial irradiation (first vertical lines) hits a fresh sample. In contrast, the following vertical lines have already seen the beam and lost material.

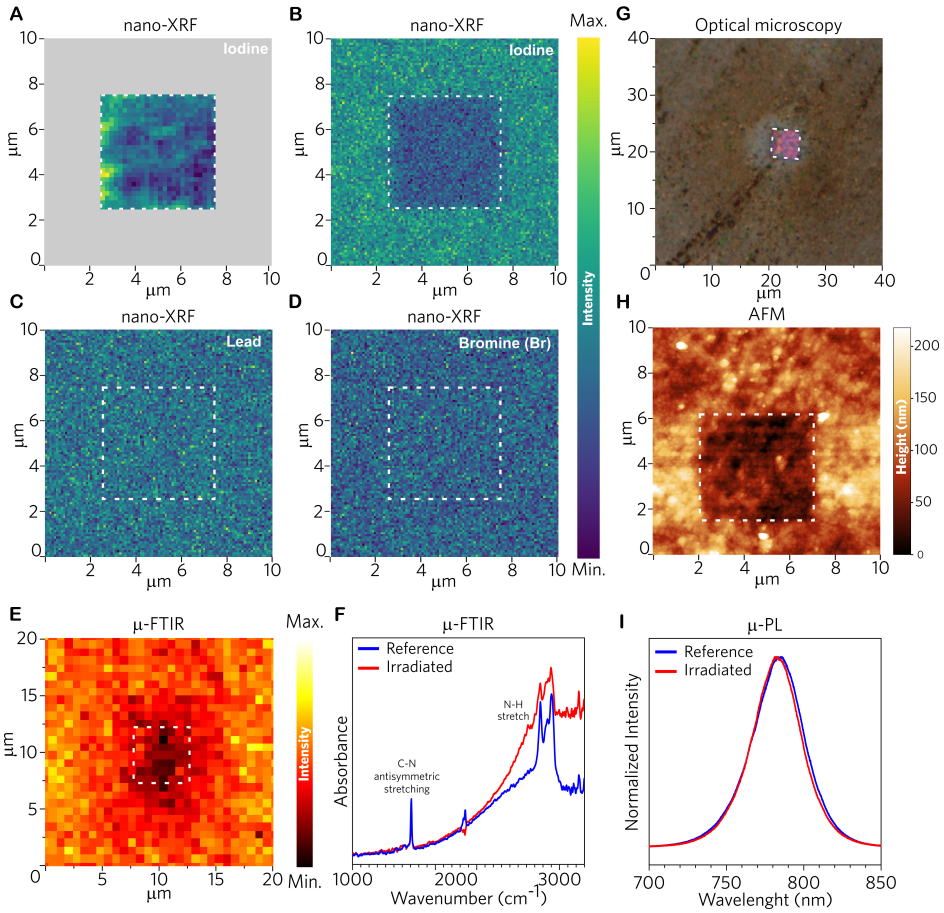

Figure 1. X-ray dose effect of raster scan in a hybrid MHP sample by an X-ray focused beam (2.9 GGy) in the air at room temperature by multiple techniques. (A) Iodine nano-XRF map collected during the high X-ray irradiation. (B-D) Iodine, lead, and bromide, respectively, nano-XRF maps of the irradiated area. (E) μ-FTIR map and (F) FTIR spectra at two different locations of the C-N antisymmetric stretching of FA (1,700 cm^{-1}). (G) optical reflectivity image of the irradiated sample. (H) AFM topography image; (I) photoluminescence spectra.

As the hybrid organic-inorganic perovskite comprises a mixture of MA and FA, which are not observable by XRF, the effect on the organic part was evaluated using μ-FTIR. Figure 1E shows a μ-FTIR map obtained by the integration of the C-N antisymmetric stretching vibration (1,700 cm^{-1}) of the FA molecules[35]. The decreased intensity in the X-ray irradiated region indicates that the organic molecules were also removed or degraded in the same area as for iodine. Comparing the complete FTIR spectra in the inner damaged region with the outer part (reference) reveals a change in the background for higher wavenumber [Figure 1F], indicating a compound with a more metallic characteristic and different refraction indices on the sample surface. This hypothesis is also qualitatively corroborated by a brighter color observed in the optical microscopy image [Figure 1G]. In addition, a scanning electron microscopy (SEM) measurement performed in a similar sample shows [Supplementary Figure 3] the damaged area. One can observe that the grain morphology is unaffected and a layer is formed on top of the MHP. The AFM measurements revealed a remarkable effect of the beam on the film topography [Figure 1H]. We observed an excavated depth in the irradiated area, corroborating the material consumption for iodine and organic molecules. We expected that the decrease in iodine and organic cations content would lead to changes in the PL peak position. Surprisingly, however, the peak in the irradiated region remained stable (in shape and position) with just a decreased intensity corresponding to a decrease in sample thickness. Figure 1I, showing the PL spectra

acquired using a μ-PL instrument with a spot size of 1 μm, indicates that the remaining perovskite compound underneath the excavated area preserves the bandgap properties. Supplementary Figure 4 shows the decrease in PL intensity through a line scan in the damaged area.

Figure 2 shows the X-ray dose effects investigated RT-Air conditions with a fixed photon flux yielding an absorbed dose rate of 4.7 KGy/s. The total irradiation time on the area of 5 × 5 μm^2 was adapted so that the samples absorbed three different dose levels: 2.9 (as in Figure 1), 1.9, and 0.7 GGy. As mentioned above, the 10 × 10 μm^2 inspection corresponds to an additional 0.2 GGy. The equivalent of 10-keV photons is given in Supplementary Table 1. The data set in Figure 2A is adapted from Figure 1 and plotted along with the two new sets with medium (1.9 GGy) and low (0.7 GGy) doses [Figure 2B and C] for comparison.

The iodine consumption attenuates as the total deposited dose reduces to 1.9 and 0.7 GGy (Figure 2B and C, respectively). Comparing the ratio between the iodine fluorescence in a 1 × 1 μm^2 area in the inner and the non-irradiated regions, we note that the highest dose leads to an iodine consumption of about 28%, attenuated to 16% at 1.9 GGy and 5% at 0.7 GGy [Figure 2D]. The last measurement is within the error bar and is barely seen on the XRF map.

Regarding the organic cations, the μ-FTIR map (Figure 2A-C, FTIR column) shows the expected tendency of diminishing the beam damage with a smaller amount of energy deposited on the sample. The dose effect is mitigated with an attenuation down to 0.7 GGy dose. The tendency is clear by evaluating the integrated profile at the 1,700 cm^{-1} resonance (C-N antisymmetric stretching) in the irradiated region, which gives about a 30% decrease for the two highest doses and is absent for the smallest one [Figure 2E]. The profile shows a reduction broader than in the irradiated area (pink column), which should come partially from the limited spatial resolution at 1,700 cm^{-1} due to the diffraction limit at this wavelength (5,882 nm). This broadening reduces at shorter wavelengths, as shown by the μ-FTIR images at the region of N-H stretching vibrations (3,100-3,400 cm^{-1}) [Supplementary Figure 5], with a sharper profile more consistent with the irradiated area.

The decrease in iodine and organic cation FA corroborates with the excavation in the irradiated area. The total thickness of the perovskite was previously measured by a profilometer to be around 330 nm. Taking the depth observed in the AFM topographic images [Supplementary Figure 6], the ratio of the excavation to the film thickness is estimated to be 27% (90 nm) and 21% (70 nm) from the highest to the intermediated dose, respectively. These ratios are comparable to the iodine attenuation shown in Figure 2D. We should point out that error bars for these measurements are within 15%, as measured by the statistical fluctuations outside the irradiated area.

These experiments were performed using the same dose rate and changing the exposition time. One can inquire which parameter is relevant, dose rate or total dose. To verify if the damage depends on the dose rate, we measured the iodine XRF signal as a function of time at a fixed sample position for two rates (1.2 and 0.23 GGy/s) at the energy of 10 keV. Figure 3A shows that the higher dose rate causes the expected faster decay in the iodine content. However, when we present the iodine consumption not as a function of time but as a function of the total absorbed dose [Figure 3B], we note that the iodine decay for both dose rates is superimposed. The decaying signal fits with two exponential components for both dose rates and gives similar decay coefficients: 972 and 28 GGy^{-1} for 1.2 GGy/s and 916 and 36 GGy^{-1} for 0.23 GGy/s, suggesting that the process occurs independently of the dose rate. A reasonable hypothesis could be that the free surface excavation is faster initially. However, as more iodine and organic molecules are knocked out, the remaining atoms at the surface, Pb and Br, form a thin coating metallic layer (evidence from FTIR broad

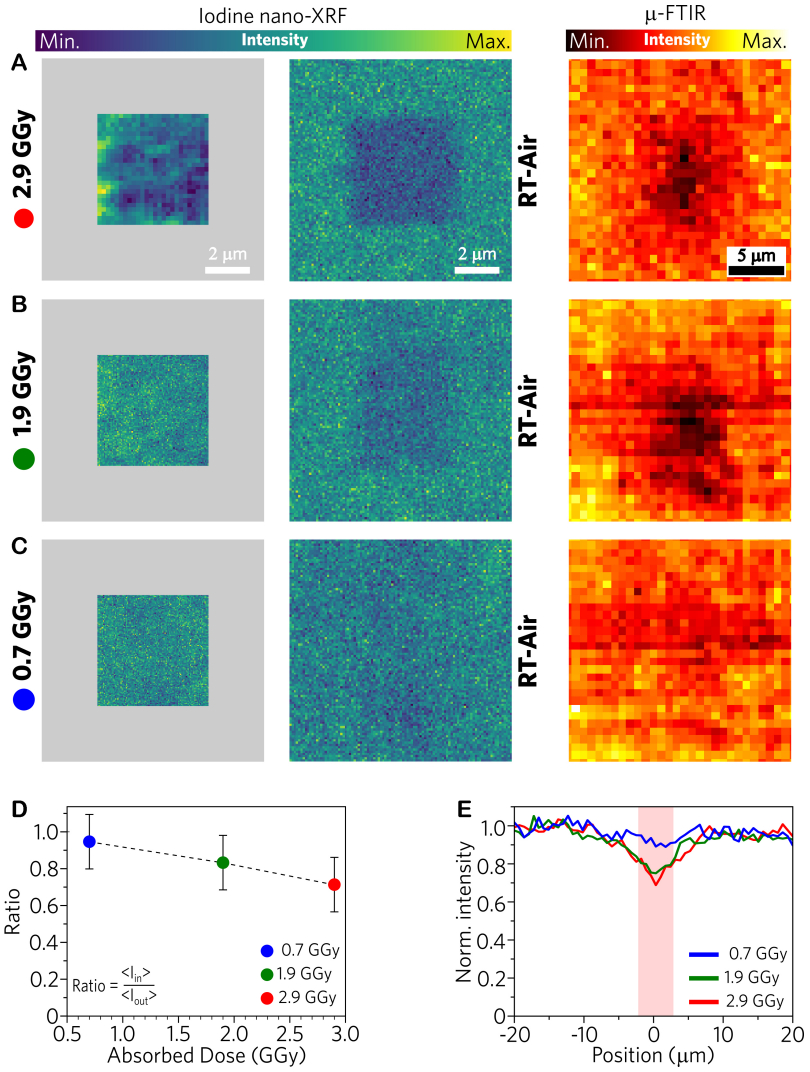

Figure 2. Absorbed X-ray dose effect for three different doses in air atmosphere. From left to right, nano-XRF irradiation, nano-XRF inspection, and C-N antisymmetric stretching μ-FTIR maps for doses of (A) 2.9 GGy, (B) 1.9 GGy, and (C) 0.7 GGy. (D) The relative decrease in the iodine content, and (E) μ-FTIR intensity.

band formed and optical images), slowing the process. Nonetheless, additional experiments are necessary to confirm this hypothesis.

This experiment demonstrates that reducing the dose rate is ineffective in mitigating beam damage in the air. What matters is the integrated absorbed dose needed to extract reliable information from the X-ray techniques. A similar experiment was performed at two photon energies, 10 and 14 keV, below and above the Pb and Br absorption edges for completeness. The X-ray fluxes were controlled to achieve the same absorbed dose rate at both energies, accounting for absorption and photon energy variation. Supplementary Figure 7 shows that the variation in iodine content is the same for both X-ray energies provided the absorbed dose is the same, corroborating the observation that the total dose absorbed by the material is the determining factor to the iodine consumption in air and at room temperature.

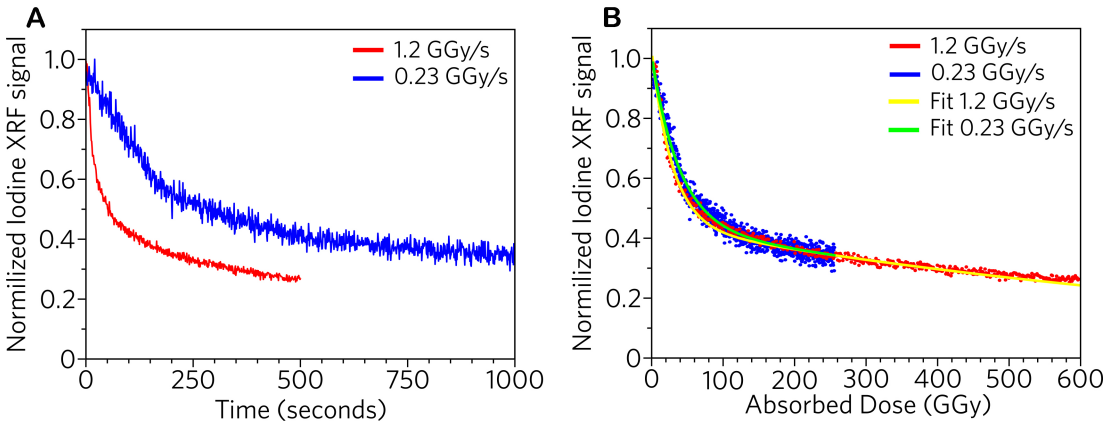

Figure 3. Effect of the absorbed dose rate on iodine signal with the X-ray beam in a fixed position for two different absorbed dose rates. (A) Normalized iodine XRF signal in function of time and (B) the dose.

The atmosphere and temperature conditions were investigated as another strategy to mitigate the beam damage. The same dose conditions (2.9, 1.9, and 0.7 GGy) were applied in three environmental situations: RT-Air, RT-N_2, and Cryo-N_2. The RT-Air condition corresponds to previously discussed measurements [Figures 1 and 2]. At the RT-N_2 condition and the highest dose of 2.9 GGy, a faint irradiated area was still observed (Figure 4A, XRF columns), yielding iodine reduced by about 16%, less than the same dose at the RT-Air condition [Figure 2]. The Cryo-N_2 condition (Figure 4B, XRF columns) seems to mitigate the effect in the XRF maps, with no observable iodine loss in the scanned region, as observed in Figure 4C (within the error bar of ±15%). The Cryo-N_2 condition seems to freeze the iodine mobility. Surprisingly, the damage persists in the organic part for both RT-N_2 and Cryo-N_2 (Figure 4A and B, μ-FTIR column), with similar intensity [Figure 4D]. The AFM topography (Figure 4A and B, AFM column, Figure 4E) confirms that the inert atmosphere does not entirely mitigate the beam excavation. An additional effect observed in the Cryo-N_2 condition is the formation of cracks in the irradiated region.

Figure 5 shows the nano-XRF and μ-FTIR of the regions measured with the smaller doses, 1.9 and 0.7 GGy, at RT-N_2. Reducing the absorbed dose and combining it with an inert atmosphere effectively mitigate the damage. The inorganic elemental distribution is stable, even if the organic component still suffers a small reduction. The topographic look-up by AFM (not shown) did not present any observable excavation. Interestingly, the PL properties are almost unaltered at the RT-N_2 condition, with a slight blueshift emission compared to the pristine sample (Figure 5C and D, column μ-PL).

The high X-ray dose (2.9 GGy) on hybrid organic-inorganic MHP produces an ion-selective ejection at the film surface, consuming iodine and organic cations but leaving Pb and Br composition unaltered, causing an excavation and altering the visible optical surface reflectivity. As expected, the X-ray dose reduction attenuates the damage, with almost complete mitigation of the consumption of iodine and organic molecules at the lowest dose (0.7 GGy) even in the air atmosphere. Under a similar dose but N_2 atmosphere, damage effects are attenuated, suggesting that the inert atmosphere is relevant to mitigating iodine loss from the sample and that the air (O_2 and H_2O) is somehow active in the iodine remotion process. The effectiveness of the N_2 atmosphere in mitigating damage has already been reported in these compounds, even though the mechanism was unclear[12]. Nevertheless, even in an inert atmosphere, there is still damage under the highest dose of 2.9 GGy. Such a critical dose should be avoided when investigating these compounds. The situation seems to be worse under cryogenic conditions. The formation of cracks in the irradiated region is probably caused by the decreased ionic mobility that helps to homogenize defects and

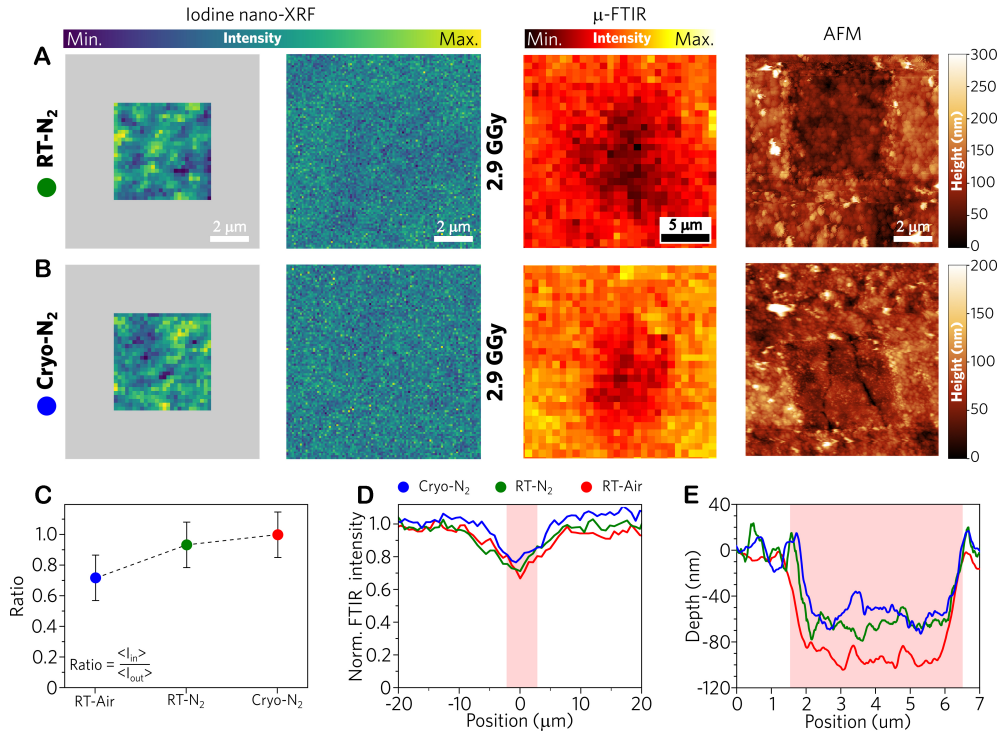

Figure 4. Effect temperature and atmosphere on damage from an X-ray dose of 2.9 GGy. From left to right, nano-XRF damage scan, nano-XRF probe scan, μ-FTIR, AFM and optical images for samples measured at (A) room temperature and nitrogen obtained by a nitrogen flow and (B) cryogenic temperature and nitrogen obtained using a cold nitrogen flow. (C) Attenuation in the iodine content, (D) μ-FTIR intensity and (E) AFM depth profiles for the different conditions.

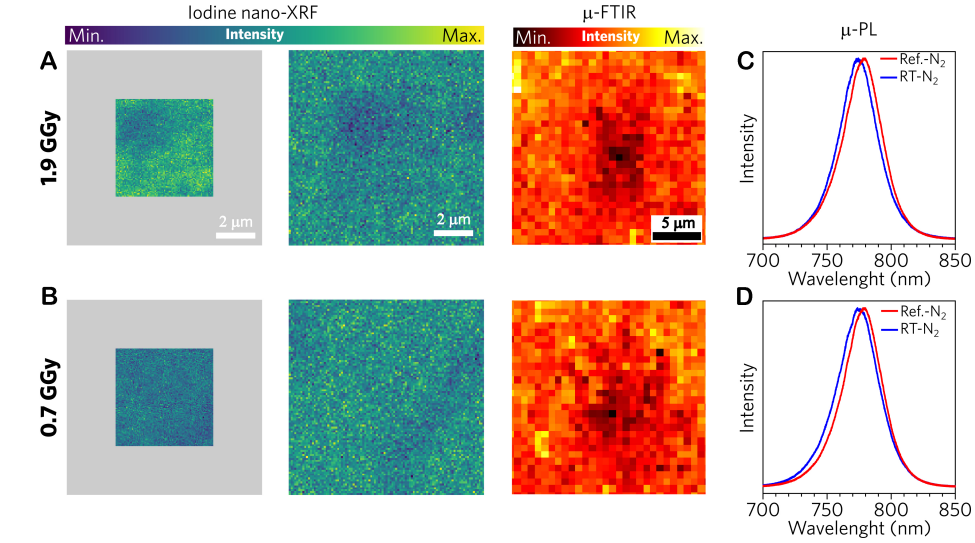

Figure 5. Perovskite damage with reduced dose and inert atmosphere. Sample irradiated with (A) 1.9 GGy and (B) 0.7 GGy in RT-N_2. From left to right, nano-XRF damage scan, nano-XRF probe scan and μ-FTIR (1,700 cm^{-1}). (C and D) Respective μ-PL at RT-N_2.

relaxes stress. Combining the intermediate dose (1.9 GGy) with N_2 atmosphere seems safe to mitigate effects and keep photovoltaic properties unaltered [Figure 5].

Figure 6 presents a schematic model for the damage caused by the X-ray beam in the organic-inorganic MHP. The X-ray absorption cross-section of the light elements, such as carbon and nitrogen from the organic part of the perovskite, is very weak, and the organic molecules are essentially transparent to the X-ray beam. On the contrary, the inorganic cage of heavy atoms absorbs the X-ray photons more efficiently, decaying through varying pathways, including the emission of a cascade of electrons that interact more effectively with the organic molecules, eventually creating ions or radicals. Both are reactive and can be neutralized or undergo reactions with another species[36,37]. Several reactions have been reported to produce new species that can be trapped in the structure or released as a gas, such as $PbBr_2$ crystallite or I_2 molecules[17,38]. This process will generate new punctual defects in the compound, eventually modifying their properties. However, if several defects are formed near each other, the 3D perovskite cage will be destroyed. Therefore, a small or intermediate dose could produce a defective material compared to a destroyed one by a severe dose.

The conservation of energy and momentum dictates that the electron must transfer energy to an atom when they interact in elastic scattering. If the transferred energy exceeds the displacement energy (E_d), the atom moves to an interstitial position, creating a defect. The E_d depends on the bond strength, crystal lattice, and atomic weight of an atom[39]. As the perovskite is composed of medium to heavy elements, an intense displacement in the bulk is not expected. However, if an atom is at the surface, the E_d is lower, and the atom can leave the specimen in a sputtering-like process[39]. One expects a high sputtering contribution from the organic molecules, independently of the atmosphere and temperature, because they are more volatiles. However, those from the inorganic elements (Pb, I, and Br) should be smaller unless they have high mobility and are more reactive, as is the case of the iodine ions exposed to the atmosphere of the air. However, even in this condition, the contribution of sputtering from inorganic elements should be smaller compared with organic molecules.

Hence, we hypothesize that the MHP damage mechanism combines radiolysis and sputtering, with the first making a larger contribution. Radiolysis produces reactive species that react with other elements, forming volatile species that leave the sample. In the air, the O_2 and H_2O molecules can react with perovskite in various ways, creating solid species such as PbO, $Pb(OH)_2$, $PbCO_3$, PbIOH, Pb, PbI_2, and $PbBr_2$[17,40,41]. Ferrer Orri *et al.* reported forming the $PbBr_2$ crystalline phase as a product after electron or X-ray irradiation[17]. Also, volatile species, such as I_2, HI, and deprotonated or degraded FA/MA molecules (CH_3I, NH_3, HCN, $C_3H_3N_3$), can form and leave the sample[42-44]. The iodine departure is corroborated by the absence of iodine accumulation at the boundaries of the 5 × 5 μm^2 irradiated area. These reactions occur close to the surface where the sputtering is more intense, and volatile molecules face a short path to escape. The N_2 atmosphere inhibits the O_2 and H_2O degradation paths. Consequently, the degradation is less severe, and inhibiting the formation of the iodine volatile species limits the iodine loss. However, the organic molecules still suffer from radiolysis and sputtering, independent of the environmental conditions.

To highlight the relevance of controlling the X-ray dose and environmental conditions when applying X-ray nanoscopy for perovskite investigation, we report an X-ray ptychography study in an MHP compound. X-ray ptychography[13] is a phase contrast technique that reveals morphological aspects not seen in traditional scanning X-ray microscopy in transmission (STXM) or XRF modes. As a phase contrast technique, ptychography is more sensitive to low-Z elements than absorption contrast techniques. We prepared and intentionally irradiated a $Cs_{0.05}FA_{0.95}PbI_3$ perovskite film, depositing a severe dose of 350 GGy on a single spot of 200 × 500 nm^2, corresponding to about 3.1 × 10^{23} 10-keV-photons/m^2. After irradiation, we performed a ptychography map on a 10 × 10 μm^2 surface with steps of 100 nm, depositing a smaller dose of 0.0015 GGy. With such a dose, observing the XRF map is possible even if the signal/noise is limited.

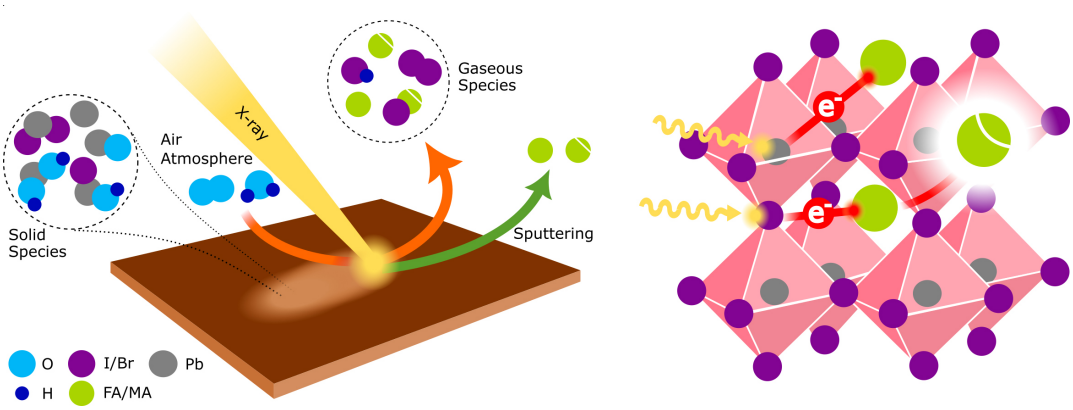

Figure 6. Schematic representation of the X-ray beam damage on the MHP.

Figure 7A shows the ptychography phase analysis, revealing the heterogeneous morphology of the sample. The calculated resolution is about 15 nm. The XRF map (integrated over iodine and cesium fluorescence emissions) collected simultaneously [Figure 7B] reveals less resolved details owing to the poorer statistics and worse spatial resolution. The inorganic damage around the damaged region can be barely seen. With X-ray ptychography, one observes a larger damaged region extending over a region bigger than 2 μm. This result means that the irradiation probably affects the organic light elements over a larger area around the irradiation position. Additionally, one can observe features such as grain morphology and some cracking that are not visible with fluorescence.

The intentional irradiation removed some iodine over an area of about 1 μm^2 but depleted the organic molecules (seen by ptychography) over a larger area than the spot size. The possibility of measuring in fly-scan mode and under a controlled dose and N_2 atmosphere was essential to mitigate eventual sample damages. The phase contrast using very low doses clearly brings new insights into the morphology and local heterogeneities of MHP compounds. Hu *et al.* reported an X-ray ptychography measurement of an inorganic perovskite $CsPb_{0.6}Sn_{0.4}I_3$ but did not discuss the resolution[45]. To our knowledge, this is the first X-ray ptychography demonstration in MHP with organic components. Ptychography is a high-sensitivity technique accessing subtle details and contrasts in sample morphology related to the material's electronic density. We foresee that our results pave the way to new correlative *in situ* and *operando* experiments with MHP. Specifically, this method is a prospect as a new probe for the early stages of degradation in MHP, including hybrid, inorganic, and Pb-free families, which were, up to now, inaccessible through other techniques.

CONCLUSIONS

Our results bring fundamental insights into the damage caused by X-ray beams on MHP compounds. We effectively applied a correlative multi-technique approach to investigate the damage caused by highly intense focused X-ray beams on hybrid organic-inorganic MHPs. By irradiating the compounds with high X-ray doses, we observed several effects that helped us understand the damage process.

Using focused X-ray beams from newly available synchrotron radiation sources for perovskite characterization will be challenging as the absorbed dose determines the damage, and each technique requires different doses to produce enough signal-to-noise ratio to extract information. Then, evaluating how the beam damage affects the desired properties as the dose increases is highly recommended before any material investigation. Our results show that combining an inert atmosphere with a controlled intermediate

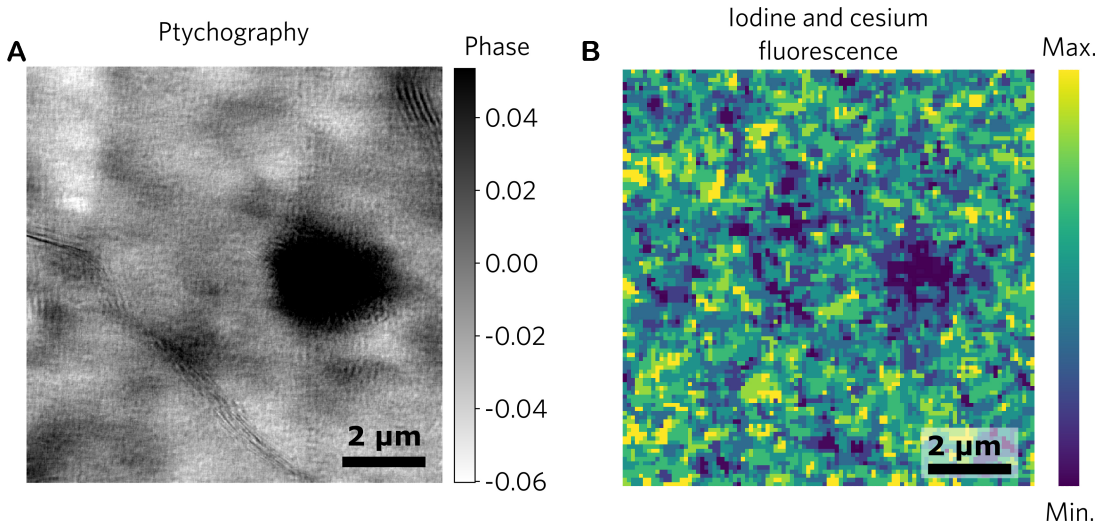

Figure 7. Simultaneous X-ray ptychography and fluorescence images of a perovskite. (A) Ptychography and (B) iodine and cesium nano-XRF images of $Cs_{0.05}FA_{0.95}PbI_3$ perovskite compound.

dose is compulsory to mitigate beam damage and provide conditions to understand the photo-structural-chemical properties of MHPs. Contrary to the expected common sense, cryogenic conditions are not the best for performing X-ray measurements under high doses because they reduce mobility and cause morphological changes. Thoroughly reporting the X-ray deposited power on samples, i.e., the absorbed dose in Gy, and environmental conditions will help the community to find the best experimental conditions to work safely.

As a clear demonstration of how powerful the use of sophisticated new techniques in synchrotron radiation facilities can be, we applied the optimized conditions below the harmful dose to demonstrate the feasibility of investigating MHPs with the X-ray ptychography technique, uncovering morphological details never seen before in MHP. Our multispectral images are a pivotal step in developing and applying the X-ray ptychography technique in beam-sensitive samples for high-resolution imaging, especially in the case of heterogeneous and hierarchical functional materials in which the multiscale properties determine final device performances.

DECLARATIONS

Acknowledgments

This research used facilities of the Brazilian Synchrotron Light Laboratory (LNLS) and Brazilian Nanotechnology National Laboratory (LNNano), part of the Brazilian Center for Research in Energy and Materials (CNPEM), a private non-profit organization under the supervision of the Brazilian Ministry for Science, Technology, and Innovations (MCTI). The CARNAUBA, IMBUIA, LAM, and LCIS facilities' staff of LNLS are acknowledged for their assistance during the beamtime and sample preparation. The facilities' staff of LNNano is acknowledged for their assistance during the profilometer and PL measurements. da Silva FMC and Guaita MGD acknowledge CNPq scholarships. Szostak R acknowledges FAPESP (Grant 2021/01357-6). The authors gratefully acknowledge support from FAPESP (Grants 2017/11986-5), Shell, and the support given by ANP (Brazil's National Oil, Natural Gas, and Biofuels Agency) through the R&D levy regulation.

Authors' contributions

Conceptualization, methodology, synchrotron and complementary experiments, data analysis and interpretation, writing the draft of the manuscript and review: da Silva FMC, Szostak S
Synchrotron experiments, sample preparation: Guaita MGD
Methodology, data discussion, review: Teixeira VC
Funding acquisition and review: Nogueira AF
Funding acquisition, review, conceptualization, methodology, and writing-review: Tolentino HCN

Availability of data and materials

Not applicable.

Financial support and sponsorship

This work was supported by FAPESP (2021/01357-6; 2017/11986-5).

Conflicts of interest

All authors declared that there are no conflicts of interest.

Ethical approval and consent to participate

Not applicable.

Consent for publication

Not applicable.

REFERENCES

1. Chen H, Maxwell A, Li C, et al. Regulating surface potential maximizes voltage in all-perovskite tandems. *Nature* 2023;613:676-81. DOI
2. Park J, Kim J, Yun HS, et al. Controlled growth of perovskite layers with volatile alkylammonium chlorides. *Nature* 2023;616:724-30. DOI
3. Kim JS, Heo JM, Park GS, et al. Ultra-bright, efficient and stable perovskite light-emitting diodes. *Nature* 2022;611:688-94. DOI
4. Sun Y, Ge L, Dai L, et al. Bright and stable perovskite light-emitting diodes in the near-infrared range. *Nature* 2023;615:830-5. DOI
5. Deumel S, van Breemen A, Gelinck G, et al. High-sensitivity high-resolution X-ray imaging with soft-sintered metal halide perovskites. *Nat Electron* 2021;4:681-8. DOI
6. Perini CA, Doherty TA, Stranks SD, Correa-baena J, Hoye RL. Pressing challenges in halide perovskite photovoltaics - from the atomic to module level. *Joule* 2021;5:1024-30. DOI
7. Szostak R, de Souza Gonçalves A, de Freitas JN, et al. In situ and operando characterizations of metal halide perovskite and solar cells: insights from lab-sized devices to upscaling processes. *Chem Rev* 2023;123:3160-236. DOI
8. Correa-Baena JP, Luo Y, Brenner TM, et al. Homogenized halides and alkali cation segregation in alloyed organic-inorganic perovskites. *Science* 2019;363:627-31. DOI
9. Frohna K, Anaya M, Macpherson S, et al. Nanoscale chemical heterogeneity dominates the optoelectronic response of alloyed perovskite solar cells. *Nat Nanotechnol* 2022;17:190-6. DOI
10. Macpherson S, Doherty TAS, Winchester AJ, et al. Local nanoscale phase impurities are degradation sites in halide perovskites. *Nature* 2022;607:294-300. DOI
11. Li N, Luo Y, Chen Z, et al. Microscopic degradation in formamidinium-cesium lead iodide perovskite solar cells under operational stressors. *Joule* 2020;4:1743-58. DOI
12. da Silva FMC, Szostak R, Teixeira VC, et al. Disentangling X-ray and sunlight irradiation effects under a controllable atmosphere in metal halide perovskites. *Solar RRL* 2023;7:2200898. DOI
13. Pfeiffer F. X-ray ptychography. *Nat Photon* 2018;12:9-17. DOI
14. Stuckelberger ME, Nietzold T, West BM, et al. Effects of X-rays on perovskite solar cells. *J Phys Chem C* 2020;124:17949-56. DOI
15. Svanström S, García Fernández A, Sloboda T, Jacobsson TJ, Rensmo H, Cappel UB. X-ray stability and degradation mechanism of lead halide perovskites and lead halides. *Phys Chem Chem Phys* 2021;23:12479-89. DOI PubMed

16. Schulz P, Whittaker-brooks LL, Macleod BA, Olson DC, Loo Y, Kahn A. Electronic level alignment in inverted organometal perovskite solar cells. *Adv Mater Inter* 2015;2:1400532. DOI
17. Ferrer Orri J, Doherty TAS, Johnstone D, et al. Unveiling the interaction mechanisms of electron and X-ray radiation with halide perovskite semiconductors using scanning nanoprobe diffraction. *Adv Mater* 2022;34:e2200383. DOI
18. Ma C, Eickemeyer FT, Lee SH, et al. Unveiling facet-dependent degradation and facet engineering for stable perovskite solar cells. *Science* 2023;379:173-8. DOI
19. Chen S, Zhang Y, Zhao J, et al. Transmission electron microscopy of organic-inorganic hybrid perovskites: myths and truths. *Sci Bull* 2020;65:1643-9. DOI
20. Rothmann MU, Li W, Zhu Y, et al. Structural and chemical changes to $CH_3NH_3PbI_3$ induced by electron and gallium ion beams. *Adv Mater* 2018;30:e1800629. DOI
21. Scalon L, Szostak R, Araújo FL, et al. Improving the stability and efficiency of perovskite solar cells by a bidentate anilinium salt. *JACS Au* 2022;2:1306-12. DOI PubMed PMC
22. Tolentino HC, Geraldes RR, da Silva FM, et al. The CARNAÚBA X-ray nanospectroscopy beamline at the Sirius-LNLS synchrotron light source: developments, commissioning, and first science at the TARUMÃ station. *J Electron Spectrosc* 2023;266:147340. DOI
23. Lena FR, Bueno CSNC, Cardoso FH, et al. Commissioning of the cryogenic sample environment for the TARUMÃ station at the CARNAÚBA beamline at Sirius/LNLS. *J Phys Conf Ser* 2022;2380:012108. DOI
24. Godden TM, Suman R, Humphry MJ, Rodenburg JM, Maiden AM. Ptychographic microscope for three-dimensional imaging. *Opt Express* 2014;22:12513-23. DOI PubMed
25. Dierolf M, Menzel A, Thibault P, et al. Ptychographic X-ray computed tomography at the nanoscale. *Nature* 2010;467:436-9. DOI
26. Vijayakumar J, Yuan H, Mille N, et al. Soft X-ray spectro-ptychography of boron nitride nanobamboos, carbon nanotubes and permalloy nanorods. *J Synchrotron Radiat* 2023;30:746-57. DOI PubMed PMC
27. Thibault P, Dierolf M, Bunk O, Menzel A, Pfeiffer F. Probe retrieval in ptychographic coherent diffractive imaging. *Ultramicroscopy* 2009;109:338-43. DOI PubMed
28. Gerchberg RW. A practical algorithm for the determination of phase from image and diffraction plane pictures. *Optik* 1972;35:237-46. Available from: https://www.scirp.org/reference/referencespapers?referenceid=2890261 [Last accessed on 3 June 2024].
29. Luke DR. Relaxed averaged alternating reflections for diffraction imaging. *Inverse Probl* 2005;21:37-50. DOI
30. Fienup JR. Phase retrieval algorithms: a comparison. *Appl Opt* 1982;21:2758-69. DOI
31. Fienup JR. Reconstruction of an object from the modulus of its Fourier transform. *Opt Lett* 1978;3:27-9. DOI PubMed
32. Liu L, Oliveira A, Tavares D, et al. Status of SIRIUS operation with users. Proceedings of the 14th international particle accelerator conference; 2023 May 7-12; Venice, Italy.
33. Kirz J, Jacobsen C, Howells M. Soft X-ray microscopes and their biological applications. *Q Rev Biophys* 1995;28:33-130. DOI PubMed
34. Jones MWM, Hare DJ, James SA, de Jonge MD, McColl G. Radiation dose limits for bioanalytical X-ray fluorescence microscopy. *Anal Chem* 2017;89:12168-75. DOI PubMed
35. Szostak R, Silva JC, Turren-Cruz SH, et al. Nanoscale mapping of chemical composition in organic-inorganic hybrid perovskite films. *Sci Adv* 2019;5:eaaw6619. DOI PubMed PMC
36. Ilett M, S'ari M, Freeman H, et al. Analysis of complex, beam-sensitive materials by transmission electron microscopy and associated techniques. *Philos Trans A Math Phys Eng Sci* 2020;378:20190601. DOI PubMed PMC
37. Stenn K, Bahr GF. Specimen damage caused by the beam of the transmission electron microscope, a correlative reconsideration. *J Ultrastruct Res* 1970;31:526-50. DOI PubMed
38. Tang X, Brandl M, May B, et al. Photoinduced degradation of methylammonium lead triiodide perovskite semiconductors. *J Mater Chem A* 2016;4:15896-903. DOI
39. Egerton RF, Li P, Malac M. Radiation damage in the TEM and SEM. *Micron* 2004;35:399-409. DOI PubMed
40. Godding JS, Ramadan AJ, Lin Y, Schutt K, Snaith HJ, Wenger B. Oxidative passivation of metal halide perovskites. *Joule* 2019;3:2716-31. DOI
41. Marchezi PE, Therézio EM, Szostak R, et al. Degradation mechanisms in mixed-cation and mixed-halide $Cs_xFA_{1-x}Pb(Br_yI_{1-y})_3$ perovskite films under ambient conditions. *J Mater Chem A* 2020;8:9302-12. DOI
42. Zhuang J, Wang J, Yan F. Review on chemical stability of lead halide perovskite solar cells. *Nanomicro Lett* 2023;15:84. DOI PubMed PMC
43. Juarez-perez EJ, Ono LK, Qi Y. Thermal degradation of formamidinium based lead halide perovskites into *sym* -triazine and hydrogen cyanide observed by coupled thermogravimetry-mass spectrometry analysis. *J Mater Chem A* 2019;7:16912-9. DOI
44. Juarez-perez EJ, Hawash Z, Raga SR, Ono LK, Qi Y. Thermal degradation of $CH_3NH_3PbI_3$ perovskite into NH_3 and CH_3I gases observed by coupled thermogravimetry-mass spectrometry analysis. *Energy Environ Sci* 2016;9:3406-10. DOI
45. Hu M, Chen M, Guo P, et al. Sub-1.4eV bandgap inorganic perovskite solar cells with long-term stability. *Nat Commun* 2020;11:151. DOI PubMed PMC